

The diurnal cycle of rainfall over New Guinea in convection-permitting WRF simulations

M. E. E. Hassim^{1,2}, T. P. Lane¹, and W. W. Grabowski³

¹School of Earth Sciences and ARC Centre of Excellence for Climate System Science,
The University of Melbourne, Melbourne, Victoria, 3010, Australia

²Now at Centre for Climate Research Singapore, Meteorological Service Singapore, Singapore

³National Center for Atmospheric Research, Boulder, Colorado, USA

Correspondence to: M. E. E. Hassim (muhammad_eeqmal_hassim@nea.gov.sg)

Abstract. In this study, we examine the diurnal cycle of rainfall over New Guinea using a series of convection-permitting numerical simulations with the Weather Research and Forecasting (WRF) model. We focus our simulations on a period of suppressed regional-scale conditions (February 2010) during which local diurnal forcings are maximised. Additionally, we focus our study on the
5 occurrence and dynamics of offshore propagating convective systems that contribute to the observed early-morning rainfall maximum north-east of New Guinea.

In general, modelled diurnal precipitation shows good agreement with satellite-observed rainfall, albeit with some timing and intensity differences. The simulations also reproduce the occurrence and variability of overnight convection that propagate offshore as organised squall lines north-east
10 of New Guinea. The occurrence of these offshore systems is largely controlled by background conditions. Days with offshore propagating convection have more middle tropospheric moisture, larger CAPE and greater low-level moisture convergence. Convection has similar characteristics over the terrain on days with and without offshore propagation.

The offshore propagating convection manifests via a multi-stage evolutionary process. First, scattered
15 convection over land, which is remnant of the daytime maximum, moves towards the coast and becomes re-organised near the region of coastal convergence associated with the land breeze. The convection then moves offshore in the form of a squall line at $\sim 5 \text{ m s}^{-1}$. In addition, cool anomalies associated with gravity waves generated by precipitating land convection propagate offshore at a dry hydrostatic gravity wave speed (of $\sim 15 \text{ m s}^{-1}$), and act to destabilise the coastal/offshore environ-
20 ment prior to the arrival of the squall line. Although the gravity wave does not appear to initiate the convection or control its propagation, it should contribute to its longevity and maintenance. The results highlight the importance of terrain and coastal effects along with gravity waves in contribut-

ing to the diurnal cycle over the Maritime Continent, especially the offshore precipitation maxima adjacent to quasi-linear coastlines.

25 1 Introduction

The diurnal cycle of rainfall is the most fundamental mode of tropical internal variability. Across the Maritime Continent (MC), convective activity is widespread, exhibiting distinct spatial patterns and strong daily contrasts between land and the surrounding seas. Precipitation over land peaks in the afternoon to early evening. Conversely, while there is relatively little amplitude in the diurnal cycle of rainfall over the open ocean, secondary rainfall maxima are seen near the coasts of many MC islands (e.g. Kikuchi and Wang, 2008).

These offshore rainfall concentrations are most prominent near the land–sea boundaries of Sumatra, Borneo, Java and New Guinea during pre-dawn hours, where sharp gradients in coastal precipitation frequencies are seen in very high-resolution data derived from the Tropical Rainfall Measuring Mission (TRMM) precipitation radar (PR) dataset (Biasutti et al., 2012). Using high-resolution brightness temperature data, Yang and Slingo (2001) noted that diurnal convective variations over the major islands (viz. New Guinea and Sumatra) spread out coherently into adjacent coastal seas over a few hundred kilometres. They speculated that seaward propagating disturbances (viz. gravity waves of varying depths) could be responsible for the signal spreading. However, the details of processes leading to offshore rainfall were not explored. More recent studies have since confirmed not only the night time offshore propagation signal, but also an afternoon inland migration from the coastline due to systems initiated along the sea breeze front (Mori et al., 2004; Zhou and Wang, 2006; Kikuchi and Wang, 2008). Both onshore and offshore rainfall features do vary with large-scale conditions, such as through variations in phase of the Madden–Julian Oscillation (e.g., see Peatman et al., 2014). However, they are persistent features nonetheless.

Notably, all the major islands in the Maritime Continent have significant topography located near the coast. The presence of steep terrain generates localised circulations in response to solar heating – in particular, upslope winds – that in turn, initiate convection over the mountains in the early afternoon (Qian, 2008). As the sea breeze develops and penetrates inland during the afternoon, superposition of the sea breeze front with upslope flows helps to feed the existing convection, promoting further development over the mountain slopes (e.g., Zhou and Wang, 2006; Wu et al., 2008; Barthlott and Kirshbaum, 2013).

However, the processes that lead to nocturnal precipitating systems over adjacent coastal seas appear to be less straightforward. For example, converging land breezes from neighbouring landmasses are proposed for cases of early morning convection seen in Van Diemen Gulf northeast of Darwin (Wapler and Lane, 2012) and over the Java sea (Qian, 2008). Meanwhile, Fujita et al. (2010) concluded that the night time rainfall maximum seen in the Strait of Malacca is due to the interac-

tion between the land breeze and downslope winds from the mountainous areas of Sumatra and the Malay Peninsula. In addition, the regular appearance of nocturnal coastal convection northwest of Borneo is attributed to surface convergence between the land breeze and the winter monsoonal flow (Houze et al., 1981) but more recently, to intense offshore surface flows due to convectively-induced boundary layer thermal gradients (Wu et al., 2008). The latter mechanism is also invoked to explain the abundance of rainfall offshore near western Sumatra (Wu et al., 2009). Finally, Love et al. (2011) demonstrate the importance of offshore propagating gravity waves in contributing to the formation of precipitation offshore. They invoke a combination of the diurnally-forced gravity waves described by Mapes et al. (2003) and convectively generated (stratiform) cooling as the source of these waves. Given the variations in spacing and the complex orientation and topography of the MC islands, it is plausible that different mechanisms may operate to produce nocturnal offshore rainfall at different coastal locations in the Maritime Continent region.

New Guinea is the largest island in the Maritime Continent. It also has the steepest and highest orography of all the major MC islands, with peaks exceeding 3000 m (Fig. 1a). The primary mountain chain forms the island’s “spine” and runs parallel to the northern coastline, which is quasi-linear and aligned in a northwest-southeast direction much like the coast of western Sumatra. A much lower ridge is situated next to the northern coast, with peaks largely between 250–750 m. The topography of New Guinea is therefore analogous to that of Sumatra in the western MC, except that Sumatra has higher mountains (≥ 1000 m) next to its western coast.

In this paper, we examine the diurnal cycle of rainfall over New Guinea using convection-permitting simulations with the Weather Research and Forecasting model (WRF). One aim of the paper is to examine the dynamics and occurrence of propagating convective signals that lead to the early-morning offshore precipitation maxima. Our focus is on a one-month period (February 2010) during the “Year of Tropical Convection” (YOTC, Moncrieff et al., 2012), which has suppressed large-scale convective conditions; this period is chosen in an attempt to isolate the localised island forcing.

The remainder of the paper is organised as follows. The next section (Sect. 2) describes the model setup and numerical experiments. Section 3 reports on the convection-permitting simulations. Analysis between occurrences of offshore rainfall propagation and times when it is lacking is discussed in Sect. 3.2, including the dynamical mechanisms associated with the convective systems over the sea. Finally, Sect. 4 provides a summary and concluding remarks.

2 WRF simulations

2.1 Model setup

Simulations are conducted using version 3.3 of the Weather Research and Forecasting model (WRF) – Advanced Research Core (WRF-ARW) (Skamarock et al., 2008) with a one-way nested configura-

tion (Fig. 1). Most of this study focuses on a two-domain setup with an outer domain (d01) that has 540 × 420 grid points with a 12 km grid spacing and a second domain (d02) consisting of 840 × 990
95 grid points and a 4 km grid spacing. The second domain is centred on the southern parts of New Guinea and covers a large portion of northern Australia; the domain includes Darwin, which is used for additional evaluation considered later. Additional simulations are also conducted with a third domain (d03) with 1.33 km grid spacing (1830 × 2190 grid points, dashed box in Fig. 1a) that is nested within d02.

100 All model domains have 80 vertical levels with a model top of 10 hPa (~ 30 km in altitude). A 10 km deep Rayleigh-friction sponge layer is used to minimize the reflection of upward-propagating gravity waves generated by convection. A stretched vertical grid is used, with grid spacing between 50–300 m in the lowest 4 km, then averaging ~ 300 m between 4–14 km before varying exponentially to 600 m by 20 km. This setup ensures reasonably high resolution in the vertical, al-
105 though many unresolved turbulent processes remain. The vertical velocity damping option is also used to prevent the model from becoming unstable with large vertical velocities over steep terrain. Initial conditions are provided by the European Centre for Medium-Range Weather Forecasts interim (ERA-Interim) reanalysis data (Dee et al., 2011) at 0.75° × 0.75° resolution. Lateral boundary conditions for the outer 12 km domain and sea-surface temperatures for all domains are prescribed
110 every 6 h from ERA-Interim data. The model time steps are 30 s for d01, 10 s for d02, and 3.3 s for d03.

The simulations utilise various physical parameterisations. These include the Noah land surface model, the Goddard scheme for shortwave radiation, the Rapid Radiative Transfer Model (RRTM) for longwave radiation and the Mellor–Yamada–Janjic (MYJ) 2.5 level planetary boundary layer
115 (PBL) scheme. The MYJ PBL scheme is used in conjunction with the Janjic Eta Monin–Obukhov surface layer scheme. Radiation calls are made every 10 min on both domains. Sub-grid scale convection in the 12 km outer domain is parametrised by the Kain–Fritsch cumulus scheme. The inner domains (d02 and d03) are considered convection-permitting and moist processes are treated explicitly. Cloud microphysical processes are represented with the WRF Single Moment 6-class (WSM6)
120 scheme.

2.2 Description of experiments and data

Unless otherwise noted, the results reported herein are from five overlapping simulations that are conducted in sequence to cover the period between 12:00 UTC, 01 February 2010 and 12:00 UTC, 28 February 2010. These overlapping simulations use d01 and d02 only. Each simulation is performed
125 separately and then concatenated to constitute the month. This period was chosen because the eastern MC region experienced suppressed regional-scale conditions coinciding with an active Madden–Julian Oscillation (MJO) phase in the Pacific Ocean in early February transitioning to an inactive

MJO in late February (M. Wheeler, personal communication, 2013); thus local diurnal forcings are maximised and sub-monthly variability can be seen.

130 The five simulations span the following timeslices: (1) 12:00 UTC, 01 February–23:00 UTC, 06 February (T1), (2) 12:00 UTC, 06 February–23:00 UTC, 11 February (T2), (3) 12:00 UTC, 11 February–23:00 UTC, 16 February (T3), (4) 12:00 UTC, 16 February–23:00 UTC, 21 February (T4), and (5) 12:00 UTC, 21 February–12:00 UTC, 28 February (T5).

135 Model output is saved hourly but the first 12 h of each simulation are regarded as spin-up and not used. Results are analysed for the period 00:00 UTC, 02 February–23:00 UTC, 27 February and only for the inner 4 km domain. A smooth contiguous span of model data for the analysis is ensured by appending consecutive timeslices such that the 23:00 UTC, 06 February data of T1 is followed by 00:00 UTC, 07 February data of T2, and 23:00 UTC, 11 February data of T2 is followed by 00:00 UTC, 12 February data of T3, etc. Note the overlap addresses the precipitation spin-up
140 problem that models generally suffer from and allows model flow fields to properly adjust to imposed boundary conditions.

The rationale of running separate timeslices with re-initialised conditions as opposed to a single, continuous run (i.e. “free-running”) for the chosen period is because previous studies show that the representation of observed events is sensitive to the initialisation time as simulations with longer
145 lead times perform poorly (e.g., Wapler et al., 2010 and Wapler and Lane, 2012). A continuous run is known to produce the lowest skill (e.g., Lo et al., 2008).

In addition to the above-described overlapping simulations, another simulation is completed with the three (one-way nested) domains for the purposes of assessing the resolution sensitivities. Because of the much higher computational cost, this setup was only run for 14 consecutive days (12:00 UTC,
150 01 February–12:00 UTC, 15 February), with the first 12 h excluded from the analysis due to spin-up issues. This is hereafter referred to as the “free-running” simulation.

A compositing technique is used to evaluate the simulated diurnal cycle, following the example of May et al. (2012). Specifically, the mean diurnal cycle is constructed by averaging all values at a particular time of day and the mean day is constructed by a series of such averages. Such an
155 approach is also used to analyse the observational data.

Modelled precipitation patterns for New Guinea are assessed with the Tropical Rainfall Measuring Mission (TRMM) 3B42 version 7 gridded rainfall dataset (Huffman et al., 2010). 3B42 data is a blended rainfall product, derived from a complex combination of TRMM precipitation radar (PR) estimates and satellite data obtained from other passive sensors (microwave and infrared). Final estimates are scaled to match monthly rain gauge values. The merged data product consists of 3 hourly
160 centred averages and has a spatial resolution of $0.25^\circ \times 0.25^\circ$, which makes it suitable to study diurnal spatial patterns of tropical rainfall. Modelled rainfall is coarse-grained to the same temporal and spatial resolution whenever it is compared to TRMM.

Rainfall observations inferred from the Darwin (Gunn Point) C-band polarimetric radar (CPOL) are also used to evaluate the model. The rainfall rates are derived from radar reflectivities using the algorithm described by Bringi et al. (2001) and calibrated against gauge measurements. The data are at 2.5 km horizontal resolution within a 150 km radius of the radar location.

3 Results

3.1 Observed and simulated diurnal features

3.1.1 Spatial distribution

The observed total rainfall over New Guinea for the period 02–28 February is presented in Fig. 2a. Most of the precipitation falls over high terrain with maxima concentrated along the slopes. Large amounts of rainfall also occur along concave coastal bights. The occurrence of these offshore maxima are attributed to the enhanced convergence effect due to the inward curvature of coastlines (Biasutti et al., 2012). Substantial rainfall accumulations are also seen near the northern coast between 139–144°, extending about 200 km offshore in the Bismarck Sea. Daily mean rates range from 8–12 mm day⁻¹ in that region. These high rainfall rates are concentrated along a relatively linear stretch of coastline where there is no enhanced localized convergence from colliding land breezes. Interestingly, the location of these rainfall rates coincides well with the offshore maximum in diurnal brightness temperature difference reported by Liberti et al. (2001) (their Fig. 4), who documented the life cycle of convective cloudiness for New Guinea using infrared satellite data. The physical mechanism responsible for that coastal rainfall maximum is discussed in Sect. 3.2.2.

The corresponding accumulated rainfall amounts simulated by WRF at 4 km is shown in Fig. 2b. These have been coarse-grained both spatially and temporally to match the TRMM 3B42 data (i.e., a 3 hourly centred average) to facilitate proper comparison. WRF captures the observed spatial distribution of rainfall, albeit with higher modelled intensity over much of the region. This is most evident over the mountain slopes, where total rainfall amounts and mean daily rates are more than double those observed by TRMM at some locations. Less bias is seen for the coastal regions, especially for our area of interest along the northern coast.

The excessive rainfall over the slopes is partly due to the horizontal grid spacing, which at 4 km is still too coarse to resolve individual convective updrafts and gives a smoothed topography. This results in wide clouds in the simulations that do not entrain as much. Nonetheless, measurements by TRMM over steep topography should also be treated with caution, when considering the model rainfall biases over elevated terrain. Recently, Matthews et al. (2013) reported that TRMM under-predicted rainfall over high-terrain by as much as 50% when compared to long-term rain-gauge station data in the New Guinea highlands. Additional results by Chen et al. (2013) show similar under-estimates of intense rainfall over high terrain (Hawaii). These studies therefore suggest that

disparity between actual and simulated amounts (at least over elevated land) may be less than is apparent from Fig. 2.

200 To evaluate the simulated rainfall further, comparisons are made between diurnal composites derived from the WRF free-running simulation, the CPOL radar-derived rainfall, and TRMM over the 150 km radius area surrounding the Darwin CPOL radar (Fig. 3). Note these composites are over a limited number of days due to missing data. The figure shows that at 4 km resolution (d02) the daily maximum rainfall rate from WRF is in good agreement with TRMM over Darwin, except the
205 model leads TRMM by a few hours. The model shows better agreement with regards to the timing of rainfall when compared to CPOL, but has larger rainfall amounts than CPOL. The CPOL underestimation is likely due to temporal sampling issues that miss the most intense rainfall events, and TRMM 3B42 is known to have issues regarding a delayed timing of rainfall compared to other rainfall products (S. Rauniyar, personal communication, 2014). This comparison provides additional
210 confidence in the simulation results and suggests that the issues over New Guinea are related to the terrain. The differences may derive from model over-production of rain on the mountain slopes, TRMM under-estimates of rainfall over terrain, or a combination of the two. In addition, WRF has a slight tendency to overproduce the early morning convection near Darwin (similar to what Wapler et al., 2010 found). This may explain why offshore precipitation to the northeast of New Guinea is
215 slightly larger than observed as shown in Fig. 2.

3.1.2 Diurnal features

The behaviour of diurnal rainfall over New Guinea is shown by Fig. 4. This figure shows time-distance (Hovmöller) plots of 3 hourly surface rainfall, averaged across the line sections seen in Fig. 1a. Month-long diagrams from TRMM and WRF are depicted in coordinated universal time
220 (UTC) (Fig. 4a and b), while the average diurnal cycle for each are shown in local time (Fig. 4c and d). The heaviest observed daily rainfall is over land and occurs along the mountain slopes rather than directly over the peaks (in both simulations and observations). On some days (e.g., 03 and 23–26 February), offshore propagation of rainfall from the northern coast is very prominent. The precipitation signal over water is largest (≥ 2.5 mm) when it appears to originate from land (Fig. 4a).
225 The regular signal suggests that most of the accumulated rainfall offshore near the northern coast during February 2010 comes mainly from organised propagating convective systems that developed over land, rather than from cells which initiate over water. Nonetheless, there are also consecutive days when little or no offshore propagation is seen, despite there being inland convection in the afternoon (e.g., 11–15 February). The behaviour of these offshore propagating convective systems
230 and the roles of gravity waves initiating or modulating them are presumably sensitive to the large-scale state (e.g., the MJO phase). This will be considered in a future publication.

The mean diurnal cycle from TRMM (Fig. 4c) shows daily rainfall being initiated in the early afternoon over the mountain ridge before intensifying and migrating downslope towards the coast

by early evening local time (LT). One signal moves southwestwards while the other signal moves
235 towards the northern coast. The northern signal maximises at midnight over the gentler slopes around
140 km inland from the coast. The signal then continues to propagate offshore from early to mid-
morning LT the next day, maximising between 60–80 km from the coast (Fig. 4c). There is also
a rainfall disturbance propagating from the coast to the mountains in the late morning and early
240 afternoon. This refers to onshore convection that develops and slowly migrates inland following the
penetration of the sea breeze. This diurnal feature is characteristic of coastal environments around
the islands of the Maritime Continent and has been documented for New Guinea in previous studies
(e.g., Zhou and Wang, 2006).

Overall, there are some notable similarities between the model and observations as WRF captures
the gross space–time structure of the observed diurnal patterns reasonably well. This includes the
245 sub-monthly variability of offshore rainfall (Fig. 4b), the inland migration of late morning/early
afternoon rainfall from the coast and the location of peak rainfall over land, i.e., the rainfall maximum
is first seen near the mountain tops before moving down the slopes (cf. Fig. 4c and d). The timing and
location of the simulated early-morning rainfall maximum offshore compares favourably to TRMM.
However, precipitation development and timing of peak rainfall over land occurs by about 3 h too
250 early in the model and modelled signals are considerably more intense over the slopes, with offshore
rainfall also too heavy. Some of these differences can be explained in the context of the comparisons
over Darwin presented earlier. Moreover, with the exception of the timing of the absolute rainfall
maximum, most of the apparent differences between the model and TRMM in Fig. 4 are related to
a difference in the rainfall intensity.

255 In our assessment, estimated phase speeds of the peak rain signal and for the broader envelope do
not differ much between TRMM and WRF in the diurnal mean (Fig. 4c–f). Furthermore, drawing a
line between the peak over land and the peak over the ocean does not properly represent the propaga-
tion speed of the systems – convection over land and over water are parts of different morphologies.
Due to likely timing/intensity bias over terrain, the peak rainfall signal from TRMM (3.3 m s^{-1})
260 moves slightly slower over land than in WRF (4.6 m s^{-1}). The faster peak signal seen offshore from
WRF (5.5 m s^{-1} compared to TRMM at 3.7 m s^{-1}) is possibly due to there being more simulated
squalls in the later part of the month. Arguably, compositing the much coarser resolution TRMM
product could also imply a slightly faster propagation speed for the broader convective envelope.
We acknowledge that propagation speed differences between TRMM and WRF could be the result
265 of simulation bias, perhaps related to errors in the convection characteristics. However, it is more
likely a combination of timing/intensity bias from the observations, simulation bias and the effect of
coarse-graining the model output. Yet, despite these biases, the timing and occurrence of the offshore
propagating rainfall is well-represented and therefore this model experiment is well-suited to study
the dynamics of the processes at play governing the offshore precipitation.

270 3.1.3 Sensitivity to model resolution

Admittedly, the 4 km horizontal grid spacing of d02 is relatively coarse and some of the differences between the simulation and the observations could be explained by these numerical issues. For example, 4 km resolution does not properly resolve the boundary layer thermals and shallow moist convection and necessitates parametrisation of these processes. Moreover, although deep convection is treated explicitly in these simulations the convective processes are not properly resolved (they are “permitted”). This should lead to convective updrafts that are too wide and intense, in-part because of the lack of explicit entrainment and the smoothed topography, which might explain the rainfall intensity bias. To consider these issues regarding model resolution, we compare the results from the 4 km (d02) and 1.33 km (d03) simulation domains from the free-running simulation. These domains can be compared directly because of the one-way nesting configuration, which uses d02 to force only the lateral boundary conditions of d03. Of course, even at 1.33 km grid spacing many of the important processes like shallow convection remain poorly resolved.

Comparison of the two-week rainfall accumulations over the area of d03, on each model’s native grid, demonstrates notable similarity between the two resolutions (Fig. 5). Both model resolutions show similar rainfall accumulations over the slopes of New Guinea, both in terms of intensity and area. Perhaps the largest difference is that the higher-resolution d03 produces slightly more rainfall immediately offshore of the northern coast.

Comparisons of the mean diurnal cycle and its spatial distribution over New Guinea from d02 and d03 (Fig. 4e and f) shows that there is limited sensitivity to the resolutions considered here. The rainfall intensity is slightly larger, for both the diurnal peak and offshore maximum, in the higher-resolution model. Thus, reducing the grid spacing to 1.33 km does not improve the biases compared to TRMM. In terms of the individual convective systems, inspection of the modelled clouds and rainfall that propagate offshore (not shown) demonstrate increased organization at higher resolution. Over Darwin (Fig. 3) there is a similar change in precipitation intensity over land, with the increased resolution leading to a slightly larger rainfall maximum. However, because of the relatively short record used in the comparisons here, many of these differences may not be representative of the actual sensitivities. For this reason, and the apparent lack of systematic improvement with higher resolution, we focus the remaining analysis on the longer simulation dataset provided by the 4 km WRF (overlapping) simulation.

300 3.2 Emergence of the offshore rainfall maximum

3.2.1 Offshore vs. NO-Offshore days

The contrast between modelled days of significant offshore rainfall and days when it is lacking warrants further attention. Here, we examine the various conditions that may explain the offshore rainfall maximum near the northern coast as seen in Fig. 2a and b. With guidance from Fig. 4a

305 and b and inspection of hourly simulated rainfall maps (not shown), we have selected days 3 and
23–26 February to form the composite of offshore rainfall propagation days (designated simply as
Offshore). Likewise, days 11–15 February are chosen to form the composite of days when offshore
propagation is absent (denoted NO-Offshore). The selected Offshore and NO-Offshore days in the
model simulation are chosen for their general agreement with TRMM data as seen in the Hovmöller
310 diagram in Fig. 4. The mean diurnal cycle of rainfall in LT for each these composites is depicted in
Fig. 6, constructed using the compositing technique described in Sect. 2.2.

The Offshore diurnal cycle is similar to the mean diurnal cycle for February (Fig. 6a), indicating
that large-scale conditions favourable for the occurrence and propagation of offshore rainfall are the
norm in day-to-day variability for the period studied. The most intense rainfall signal near the coast
315 has a coherent propagation that begins about 50 km inland and extends about 120 km offshore. The
speed of the strongest signal (marked on Fig. 6a) is about 4.7 m s^{-1} , while the speed corresponding
to the rainfall onset is around 8 m s^{-1} (see Fig. 12b also). This value corresponds to the propagation
speed of the “gust-front” mode identified by Tulich and Mapes (2008) in their two-dimensional cloud-
resolving study. We discuss the significance of this mode in Sect. 3.2.3.

320 The rainfall patterns closer to the terrain peak move slower, but have less coherent propagation
characteristics. During NO-Offshore days (Fig. 6b) the rainfall near the terrain peak shows similar
characteristics to Offshore days, albeit with slightly slower propagation speeds, but terminates within
about 100 km of the coast. While some rain can be seen more than 120 km offshore between 03:00–
09:00 LT, the signal does not appear to follow coherent propagation from land as it does in the
325 Offshore days. This may be a signal of the open ocean diurnal cycle and not related to offshore
propagation per se.

Inspection of the environmental conditions averaged for a box region around the northern coast
provides us with an explanation for the difference in convective behaviour during Offshore days com-
pared to NO-Offshore. Figure 7a shows the mean profiles of simulated temperature and dewpoint,
330 along with parcel temperatures for Offshore and NO-Offshore days for the area within the denoted
red box. The wind components normal and parallel to the terrain, water vapour, and equivalent po-
tential temperature are also shown (Fig. 7b–d). The plot shows that both Offshore and NO-Offshore
days possess minor differences in their temperature profiles, but NO-Offshore days are much drier
especially above 700 hPa ($\sim 3 \text{ km}$) as shown by the large dewpoint depression (Fig. 7a), and large
335 differences in water vapour and equivalent potential temperature at around 6 km (Fig. 7c and d). In
fact, the middle troposphere on NO-Offshore days has a lower water vapour content than the monthly
mean, compared to Offshore days when it is anomalously moister (Fig. 7c). The coastal/offshore en-
vironment on NO-Offshore days is therefore less likely to support deep convection at night, despite
having moderate Convective Available Potential Energy (CAPE, $\sim 1400 \text{ J kg}^{-1}$). This is evident in
340 the much shallower cloud layer for the region near the northern coast on NO-Offshore days (see
Fig. 11 later). In contrast, considerably larger CAPE exists on Offshore days ($\sim 2100 \text{ J kg}^{-1}$).

The mean wind profiles normal to the coast show little variation in low-level wind speed below 500 m, which is directed onshore, or shear below 3 km, which is directed offshore. Shear values between 1–3 km are 0.0025 s^{-1} and 0.00235 s^{-1} on NO-Offshore and Offshore days, respectively. 345 There is stronger shear above 6 km in Offshore cases. Notably, there are speed and directional differences at low-levels for wind parallel to the northern coast. These could have an important effect on the moisture flux convergence in the boundary layer along the coast.

To examine the evolution of low-level moisture supply over the northern coast on both Offshore and NO-Offshore days, we calculate the total horizontal moisture flux convergence (or simply moisture convergence) by summing all grid points between the surface and a height of about 1 km (first 350 11 models levels) in the region denoted by the red box (see inset in Fig. 7a). We define this vertically-integrated moisture convergence (VIMFC) using:

$$\text{VIMFC} = - \int_{z=\text{sfc}}^{z=1 \text{ km}} [\nabla \cdot (q\mathbf{V})] \quad (1)$$

where q = specific humidity (g kg^{-1}) and \mathbf{V} = vector wind (m s^{-1}). The divergence at each grid 355 point is approximated using centred finite differences. Both Offshore and NO-Offshore days feature a significant diurnal cycle in moisture convergence, with maximum in the evening/early morning (Fig. 8). The VIMFC on Offshore days is substantially larger than on NO-Offshore days and precedes the rainfall maximum by a few hours. Most of this VIMFC difference can be attributed to the difference in boundary layer mass convergence since mean moisture content in the first 1 km is 360 similar on NO-Offshore and Offshore days (Fig. 7a). Of course, some of the VIMFC differences, especially in the hours that correspond to the coastal rainfall, may be convectively induced. However, it is important to note that during the mid-afternoon (around 15:00 LT) when both the Offshore and NO-Offshore days have active convection, the Offshore days have almost zero convergence whereas the NO-Offshore case is divergent. This suggests that regional-scale conditions, whether they be 365 boundary layer convergence or mid-level moisture (as discussed above), are playing an important role in delineating Offshore from NO-Offshore days. Arguably, the substantially larger CAPE on Offshore days is due to the increased boundary layer moisture convergence between 1500 LT and midnight (Fig. 8).

In order to isolate the convectively-generated perturbations (gravity wave) response from that 370 solely due to the diurnal heating and cooling of the elevated land, we performed an additional sensitivity experiment in which temperature tendencies from cloud microphysical processes were disabled (i.e., a dry simulation with no latent heating) to isolate the role of the heated terrain. This “dry simulation” was conducted for the period spanning 12:00 UTC, 01 February to 23:00 UTC, 04 February 2010. The same input and boundary conditions are used as before. Again, the first 12 h are 375 discarded and hourly data for days 02–04 February are composited for analysis. Results from this dry simulation are also shown in Fig. 8 and demonstrate a significantly reduced diurnal cycle compared to the results from Offshore and NO-Offshore days. This suggests that much of the diurnal cycle in

moisture convergence seen in the full physics simulations is convectively induced. Nonetheless, the differences in background environmental conditions around the northern coast between Offshore and
380 NO-Offshore days are highly suggestive of large-scale controls on the occurrence of these offshore propagating systems.

3.2.2 Propagating squall-line

As exemplified by Fig. 4a the temporal evolution of the offshore propagating convective system manifests through a multi-stage process. First, convective systems form over the peaks and move slowly
385 downslope in the early evening. Around this time the intensity of the rainfall increases as systems become more organised. Just after midnight, the convective systems reform near the coast and begin to propagate offshore at around 5 m s^{-1} . This process of system re-organisation, coastal orientation and propagation offshore is illustrated by Fig. 9 for a representative event (03 February 2010).

The vertical structure and system-relative flow for the same event post-midnight is shown in
390 Fig. 10. There is a large cloud mass over land as well as an isolated convective system near the coast. These systems merge by 02:00 LT. At 06:00 LT the convective system has evolved into a large squall line. The squall line approximately corresponds to the standard leading-line trailing stratiform archetype (e.g. Houze, 2004). The system relative wind features a stagnation point at the surface – identifying the leading edge of a propagating surface cold pool, middle-level inflow that is linked
395 with rearward directed upper level outflow, and rear-to-front flow below the anvil characteristic of a mesoscale downdraft.

3.2.3 Gravity waves

Previous studies (e.g., Mapes et al., 2003; Love et al., 2011) have explained cases of offshore propagating convective systems in the tropics as a result of gravity wave processes. This is because in
400 those cases, the systems extended further and/or faster than would be expected for land breezes or katabatic winds generated by the terrain. Mapes et al. (2003) described a mechanism for the formation of offshore convection as a result of diurnally forced gravity waves that are generated primarily by the boundary layer heating and cooling over the elevated terrain. The nocturnal phase of these waves was shown to propagate offshore at about 15 m s^{-1} and destabilise the environment, which
405 promoted convective development. Love et al. (2011) considered this further and argued that stratiform cooling from convective systems over land was an important contributor to the generation of these waves. However, as shown previously, the most intense rainfall signal from offshore convective systems herein propagates at about 5 m s^{-1} , which is considerably slower than the gravity waves considered by previous studies; instead the offshore propagating systems appear as squall
410 lines maintained by a surface cold pool. Indeed, Tulich and Mapes (2008) showed that surface-based cold pools move between $3\text{--}7 \text{ m s}^{-1}$. In this section, we consider these mechanisms further to help

understand if gravity waves play any role in the dynamics of the offshore propagating convection seen in the simulations.

Figure 11 shows vertical cross-sections of temperature perturbations that propagate from the terrain. Both Offshore and NO-Offshore days show very similar structures. At 15:00 LT, daytime boundary layer heating is evident over land, extending primarily to the depth of the terrain peak. There is an associated temperature perturbation, viz. a gravity wave, that extends offshore but is deeper; at the rightmost limits of the shown diagrams manifests as a wave structure with a vertical wavelength equal to about 10 km. (Such a wavelength is often referred to as the “ $n = 3$ wave”, as here it corresponds to three antinodes within the troposphere that extends to a depth of about 15 km in our case). By 23:00 LT the opposite phase of this wave is evident offshore, i.e., heating overlying cooling; the cooling is linked directly to the depth of precipitation below the melting level over land, as shown by the 0.05 g kg^{-1} rain mixing ratio contour. That is, the cool anomaly appears to be generated by the evaporative cooling associated with the land-based convection. Note that the wave structure is not purely sinusoidal since the lower half-wavelength has the strongest amplitude. Arguably, what the simulated convection is really setting is a strong 5 km deep cold anomaly near the surface with weaker alternating sign anomalies aloft. At 03:00 LT, when the convective system is mature and propagating offshore, the temperature anomalies are mostly negative offshore but there is still evidence of the low-level (about 4 km deep) cool anomaly extending well ahead of the convection. The cool low-level gravity wave anomalies that propagate offshore have the potential to destabilise the offshore environment and promote or initiate further convection. Previous studies (e.g., Lane and Reeder, 2001; Mapes, 1993) have shown how deep convection acts to excite these gravity waves – termed the “slow mode” by Tulich et al. (2007) – in the forward environment.

To consider the time evolution of the offshore environment associated with the passage of the gravity waves, consider time-height sections of CAPE, rainfall, and 3 km temperature perturbation (Fig. 12). Here 3 km is chosen as it is the approximate depth of the maximum cool anomaly in Fig. 11 at 03:00 LT. Red lines overlaid on the images mark the onset of offshore rainfall (cf. Fig. 12b), and blue lines mark the transition from the warm to cool anomaly offshore (cf. Fig. 12c).

The propagation of the gravity wave signal is evident in Fig. 12c, with the offshore temperature anomaly possessing a diurnal period and coherent offshore propagation at a speed of approximately 15 m s^{-1} . The phase speed of a hydrostatic gravity wave is $c = N\lambda_z/2\pi + U$, where N is the Brunt-Väisälä frequency, λ_z is the vertical wavelength, and U is the mean horizontal flow. For values of $N \approx 0.01 \text{ s}^{-1}$ and neglecting the mean low-level flow (which is only a few m s^{-1}), this 15 m s^{-1} phase speed corresponds to an approximate vertical wavelength of 10 km, which matches those waves in Fig. 11. (Incidentally, this is also the speed of the cool anomalies considered by Mapes et al. (2003)).

Of relevance, the onset of the cool gravity wave anomaly offshore corresponds to a notable increase in the CAPE that peaks during the passage of the cool anomaly. That is, the offshore prop-

agating gravity wave has destabilised the offshore environment by decreasing the environmental
450 (virtual) temperature at lower altitudes. This, coupled with the concurrent increase in boundary layer
moisture convergence (c.f. Fig. 8) explains the strong growth in CAPE offshore. During the cool
anomaly, the offshore propagating squall line propagates into this destabilised offshore environment
(albeit at a speed slower than the gravity wave); the onset of rainfall occurs within the cold wave
anomaly where that CAPE is increased. Thus, from these and results presented earlier it appears that
455 the convective system (maintained by the surface cold pool) is not initiated by the gravity wave mode
but instead the system moves into an environment that has been destabilised by the cool phase of the
gravity wave shortly before its arrival. Thus, the wave may play a role in enhancing the squall line
and promoting its longevity, but ultimately the squall line appears to originally form independent of
the wave. Nevertheless, the phase speed corresponding to the rainfall onset (8 m s^{-1}) suggests pref-
460 erential triggering of convection ahead of the main squall line. Such a phase speed is reminiscent of
the “gust-front mode” identified by Tulich and Mapes (2008), who demonstrated the efficacy of this
shallow gravity wave mode in initiating subsequent convection ahead. Inspection of Fig. 10 does in-
dicate vertical wavelength structures of about 4–5 km both within and ahead of the main convective
line. This is consistent with the short vertical wavelength of the “gust-front” mode ($\sim 5 \text{ km}$). Fur-
465 thermore, the cool temperature anomalies in the lower free troposphere ahead of the system depict
a local minimum at $\sim 1 \text{ km}$ (Fig. 11, leftmost bottom two panels). Again, this is consistent with the
temperature structures shown by Tulich and Mapes (2008) for the “gust-front” mode (their Fig. 3b),
suggesting the likely importance of this mode for triggering convection.

To consider the relative roles of the topographic and boundary layer heating/cooling vs. the dia-
470 batic forcing from convection in generating the gravity waves, results from the dry simulation are
considered here. For the dry simulation (Fig. 12d) the cooling over land is larger than the full physics
simulation, presumably due to increased nocturnal radiative cooling in the absence of clouds. Also,
because boundary layer heating and cooling extends all the way to the coast, the anomalies over
land appear stationary, fluctuating in phase with the diurnal cycle. In contrast, the offshore propagat-
475 ing gravity wave signal is substantially weaker in amplitude with a slower propagation speed. This
slower speed is consistent with the shallower cold anomaly (shorter gravity wave vertical wave-
length) seen in Fig. 11. These results strongly suggest the importance of the convective diabatic
forcing, in this case “stratiform cooling”, in contributing to the generation of the offshore prop-
agating gravity waves that further destabilise the environment (consistent with the conclusions of
480 Love et al., 2011). Nonetheless, boundary layer cooling (cf. Mapes et al., 2003) does force offshore
propagating waves that work in concert with the convectively generated waves.

As suggested by Fig. 11, the strength and depth of the offshore cool anomalies are very similar
for Offshore and NO-Offshore days. Similar time-distance analysis to Fig. 12 for NO-Offshore (not
shown) demonstrates much similarity to Offshore, including an increase in CAPE with the passage
485 of the wave of similar magnitude. Though recall in the NO-Offshore case, the background CAPE is

substantially smaller than in Offshore due to less boundary layer convergence. This result suggests that the convection over land, which occurs in both cases, plays a key role in the wave generation.

4 Conclusions

This study has examined the diurnal cycle of rainfall over New Guinea using a series of convection-permitting model simulations using the Weather Research and Forecasting (WRF) model. The simulations focus on February 2010, which is a period of suppressed regional-scale conditions chosen to maximise the local influence on the diurnal cycle. The primary focus of the study and analysis was on the occurrence and dynamics of the offshore propagating convective systems that contribute to the early-morning precipitation maximum to the northeast of New Guinea.

The model simulations are configured with one-way nested domains, with the primary focus on results from a 4 km horizontal grid spacing domain. The modelled precipitation shows good spatial agreement with observed rainfall from the TRMM 3B42 product. However, the intensity of the modelled precipitation is larger than TRMM over the steep terrain. Better agreement between the model and the observations is found over Darwin, which has substantially lower topography than New Guinea. Additional simulations, over a two-week period, using 1.33 km grid spacing show similar results and biases to the 4 km domain and lend support to using the 4 km domain over the month-long period.

The model simulations reproduce the occurrence and variability of convective systems that propagate offshore, to the northeast, of New Guinea during the night and early morning. These systems are linked to daytime convective systems over land, which reform near the coast around midnight and then propagate at about 5 m s^{-1} offshore as organised squall lines. The occurrence of the offshore systems is largely related to the background conditions. Days with offshore propagating convection have more middle tropospheric moisture, larger CAPE, and greater low-level moisture convergence than days without offshore propagating convection. Convection has similar characteristics over the terrain on both days with and without offshore propagation.

Gravity waves are also generated as part of the diurnal cycle and propagate offshore at about 15 m s^{-1} . The cool phase of these waves (with negative low-level temperature anomalies) propagates offshore during the evening and early morning, which destabilises the offshore environment (increases the CAPE) immediately prior to the arrival of the organised convective systems. The forcing of the gravity waves is linked to precipitating convection over land because an additional experiment with no convection (*viz.* a dry simulation) shows weaker and slower gravity waves. The 15 m s^{-1} gravity wave does not initiate convection *per se* and it propagates faster than the squall lines, but by increasing the CAPE the wave makes the nocturnal offshore environment more conducive to deep convection and likely contributes to the longevity of the offshore-propagating squall

520 line. However, it is possible that convection may be triggered by a “gust-front” mode moving slower at 8 m s^{-1} and corresponds to the offshore rainfall onset.

These results highlight the importance of terrain and coastal effects and gravity waves in controlling the diurnal cycle over the Maritime Continent, especially the offshore precipitation maxima. However, these results have been limited in their scope as they only focus on one period of suppressed regional-scale activity due to an active MJO phase in the eastern Pacific/western hemisphere. 525 The simulations are also only “convection-permitting” and therefore do not necessarily resolve all the processes at play. Indeed, the structure of the diurnal cycle in the Maritime Continent and its variation with the passage of the MJO has been the focus of recent work (Peatman et al., 2014). In the context of offshore propagation and its sensitivity to MJO phase, our future work will focus on 530 cases with different regional-scale conditions and higher model resolution.

Acknowledgements. The authors would like to acknowledge David Lee (formerly of The University of Melbourne, now at Los Alamos National Laboratory) for providing Fig. 3. The authors would also like to thank Tim Dunkerton (editor), Stefan Tulich, Mitchell Moncrieff and an anonymous reviewer for helpful comments which improved the quality of the manuscript. This research was supported by the ARC Centre of Excellence for Climate System Science(CE1100010128). High-performance computing was provided by the National 535 Computational Infrastructure (NCI) facility. Data analysis and visualization were conducted with The NCAR Command Language (Version 6.2.1) [Software]. (2014). Boulder, Colorado: UCAR/NCAR/CISL/VETS. doi:10.5065/D6WD3XH5

References

- 540 Barthlott, C. and Kirshbaum, D. J.: Sensitivity of deep convection to terrain forcing over mediterranean islands, *Q. J. Roy. Meteor. Soc.*, 139, 1762–1779, doi:10.1002/qj.2089, 2013.
- Biasutti, M., Yuter, S. E., Burleyson, C. D., and Sobel, A. H.: Very high resolution rainfall patterns measured by TRMM precipitation radar: seasonal and diurnal cycles, *Clim. Dynam.*, 39, 239–258, doi:10.1007/s00382-011-1146-6, 2012.
- 545 Bringi, V. N., Huang, G. J., Chandrasekar, V., and Keenan, T. D.: An areal rainfall estimator using differential propagation phase: Evaluation using a C-band radar and a dense gauge network in the tropics, *J. Atmos. Ocean. Tech.*, 18, 1810–1818, doi:10.1175/1520-0426(2001)018<1810:AAREUD>2.0.CO;2, 2001.
- Chen, Y., Ebert, E. E., Walsh, K. J. E., and Davidson, N. E.: Evaluation of TRMM 3B42 precipitation estimates of tropical cyclone rainfall using PACRAIN data, *J. Geophys. Res.-Atmos.*, 118, 2184–2196, doi:10.1002/jgrd.50250, 2013.
- 550 Dee, D. P., Uppala, S. M., Simmons, A. J., Berrisford, P., Poli, P., Kobayashi, S., Andrae, U., Balmaseda, M. A., Balsamo, G., Bauer, P., Bechtold, P., Beljaars, A. C. M., van de Berg, L., Bidlot, J., Bormann, N., Del-sol, C., Dragani, R., Fuentes, M., Geer, A. J., Haimberger, L., Healy, S. B., Hersbach, H., Hólm, E. V., Isaksen, I., Kållberg, P., Köhler, M., Matricardi, M., McNally, A. P., Monge-Sanz, B. M., Morcrette, J.-J., Park, B.-K., Peubey, C., de Rosnay, P., Tavolato, C., Thépaut, J.-N., and Vitart, F.: The ERA-Interim reanalysis: configuration and performance of the data assimilation system, *Q. J. Roy. Meteor. Soc.*, 137, 553–597, doi:10.1002/qj.828, 2011.
- Fujita, M., Kimura, F., and Yoshizaki, M.: Morning precipitation peak over the Strait of Malacca under a calm condition, *Mon. Weather Rev.*, 138, 1474–1486, doi:10.1175/2009MWR3068.1, 2010.
- 560 Houze, R. A.: Mesoscale convective systems, *Rev. Geophys.*, 42, RG4003, doi:10.1029/2004RG000150, 2004.
- Houze, R. A., Geotis, S. G., Marks, F. D., and West, A. K.: Winter monsoon convection in the vicinity of North Borneo. Part I: Structure and time variation of the clouds and precipitation, *Mon. Weather Rev.*, 109, 1595–1614, doi:10.1175/1520-0493(1981)109<1595:WMCITV>2.0.CO;2, 1981.
- Huffman, G. J., Adler, R. F., Bolvin, D. T., and Nelkin, E. J.: The TRMM Multi-satellite Precipitation Analysis (TMPA), in: *Satellite Rainfall Applications for Surface Hydrology*, chap. 1, edited by: Hossain, F. and Gebremichael, M., Springer Verlag, 3–22, 2010.
- 565 Kikuchi, K. and Wang, B.: Diurnal precipitation regimes in the global tropics, *J. Climate*, 21, 2680–2696, doi:10.1175/2007JCLI2051.1, 2008.
- Lane, T. P. and Reeder, M. J.: Convectively generated gravity waves and their effect on the cloud environment, *J. Atmos. Sci.*, 58, 2427–2440, doi:10.1175/1520-0469(2001)058<2427:CGGWAT>2.0.CO;2, 2001.
- 570 Liberti, G. L., Chéruy, F., and Desbois, M.: Land effect on the diurnal cycle of clouds over the TOGA COARE area, as observed from GMS IR data, *Mon. Weather Rev.*, 129, 1500–1517, doi:10.1175/1520-0493(2001)129<1500:LEOTDC>2.0.CO;2, 2001.
- Lo, J. C.-F., Yang, Z.-L., and Pielke Sr., R. A.: Assessment of three dynamical climate downscaling methods using the Weather Research and Forecasting (WRF) model, *J. Geophys. Res.*, 113, D09112, doi:10.1029/2007JD009216, 2008.
- 575 Love, B. S., Matthews, A. J., and Lister, G. M. S.: The diurnal cycle of precipitation over the Maritime Continent in a high-resolution atmospheric model, *Q. J. Roy. Meteor. Soc.*, 137, 934–947, doi:10.1002/qj.809, 2011.

- Mapes, B. E.: Gregarious tropical convection, *J. Atmos. Sci.*, 50, 2026–2037, doi:10.1175/1520-0469(1993)050<2026:GTC>2.0.CO;2, 1993.
- 580 Mapes, B. E., Warner, T. T., and Xu, M.: Diurnal patterns of rainfall in Northwestern South America. Part III: Diurnal gravity waves and nocturnal convection offshore, *Mon. Weather Rev.*, 131, 830–844, doi:10.1175/1520-0493(2003)131<0830:DPORIN>2.0.CO;2, 2003.
- Matthews, A. J., Pickup, G., Peatman, S. C., Clews, P., and Martin, J.: The effect of the Madden–Julian oscillation on station rainfall and river level in the Fly River system, Papua New Guinea, *J. Geophys. Res.-Atmos.*, 118, 10926–10935, doi:10.1002/jgrd.50865, 2013.
- 585 May, P. T., Long, C. N., and Protat, A.: The diurnal cycle of the boundary layer, convection, clouds, and surface radiation in a coastal monsoon environment (Darwin, Australia), *J. Climate*, 25, 5309–5326, doi:10.1175/JCLI-D-11-00538.1, 2012.
- 590 Moncrieff, M. W., Waliser, D. E., Miller, M. J., Shapiro, M. A., Asrar, G. R., and Caughey, J.: Multiscale convective organization and the YOTC virtual global field campaign, *B. Am. Meteorol. Soc.*, 93, 1171–1187, doi:10.1175/BAMS-D-11-00233.1, 2012.
- Mori, S., June-Ichi, H., Tauhid, Y. I., Yamanaka, M. D., Okamoto, N., Murata, F., Sakurai, N., Hashiguchi, H., and Sribimawati, T.: Diurnal land–sea rainfall peak migration over Sumatera Island, Indonesian Maritime 595 Continent, observed by TRMM satellite and intensive rawinsonde soundings, *Mon. Weather Rev.*, 132, 2021–2039, doi:10.1175/1520-0493(2004)132<2021:DLRPMO>2.0.CO;2, 2004.
- Peatman, S. C., Matthews, A. J., and Stevens, D. P.: Propagation of the Madden–Julian oscillation through the Maritime Continent and scale interaction with the diurnal cycle of precipitation, *Q. J. Roy. Meteor. Soc.*, 140, 814–825, doi:10.1002/qj.2161, 2014.
- 600 Qian, J.-H.: Why precipitation is mostly concentrated over islands in the Maritime Continent, *J. Atmos. Sci.*, 65, 1428–1441, doi:10.1175/2007JAS2422.1, 2008.
- Skamarock, W. C., Klemp, J. B., Dudhia, J., Gill, D. O., Baker, D. M., Duda, M. G., Huang, X.-Y., Wang, W., and Powers, J. G.: A Description of the Advanced Research WRF Version 3, NCAR/TN-47, 113 pp., 2008.
- Tulich, S. N. and Mapes, B. E.: Multiscale convective wave disturbances in the tropics: insights from a two- 605 dimensional cloud-resolving model, *J. Atmos. Sci.*, 65, 140–155, doi:10.1175/2007JAS2353.1, 2008.
- Tulich, S. N., Randall, D. A., and Mapes, B. E.: Vertical-mode and cloud decomposition of large-scale convectively coupled gravity waves in a two-dimensional cloud-resolving model, *J. Atmos. Sci.*, 64, 1210–1229, doi:10.1175/JAS3884.1, 2007.
- Wapler, K. and Lane, T. P.: A case of offshore convective initiation by interacting land breezes near Darwin, 610 Australia, *Meteorol. Atmos. Phys.*, 115, 123–137, doi:10.1007/s00703-011-0180-6, 2012.
- Wapler, K., Lane, T. P., May, P. T., Jakob, C., Manton, M. J., and Siems, S. T.: Cloud-system-resolving model simulations of tropical cloud systems observed during the Tropical Warm Pool-International Cloud Experiment, *Mon. Weather Rev.*, 138, 55–73, doi:10.1175/2009MWR2993.1, 2010.
- Wu, P., Manabu, D., and Matsumoto, J.: The formation of nocturnal rainfall offshore from convection over 615 western Kalimantan (Borneo) Island, *J. Meteorol. Soc. Jpn.*, 86A, 187–203, doi:10.2151/jmsj.86A.187, 2008.
- Wu, P., Hara, M., Hamada, J.-I., Yamanaka, M. D., and Kimura, F.: Why a large amount of rain falls over the sea in the vicinity of Western Sumatra Island during nighttime, *J. Appl. Meteorol. Clim.*, 48, 1345–1361, doi:10.1175/2009JAMC2052.1, 2009.

- 620 Yang, G.-Y. and Slingo, J.: The diurnal cycle in the tropics, *Mon. Weather Rev.*, 129, 784–801,
doi:10.1175/1520-0493(2001)129<0784:TDCITT>2.0.CO;2, 2001.
- Zhou, L. and Wang, Y.: Tropical Rainfall Measuring Mission observation and regional model study of precipitation diurnal cycle in the New Guinean region, *J. Geophys. Res.*, 111, 1–18, doi:10.1029/2006JD007243, 2006.

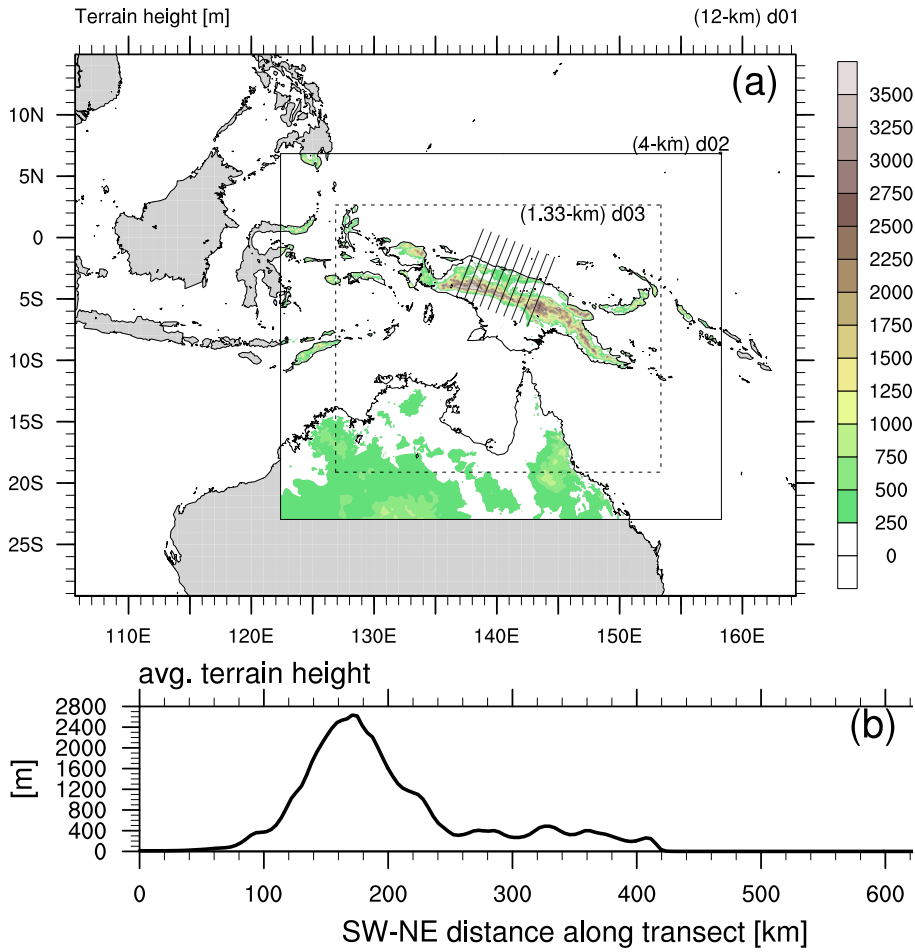


Figure 1. (a) Model domains and orography. The profile shown in (b) represents the mean terrain height (m), as averaged across the line sections shown in (a).

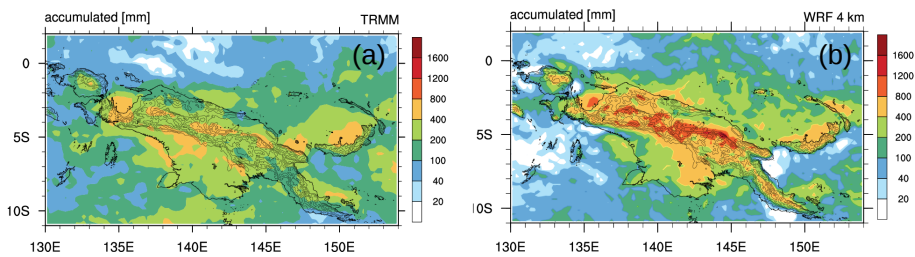


Figure 2. Accumulated rainfall (mm) for the New Guinea region between 02–28 February 2010 from TRMM (a) and the 4 km WRF simulation (b). Data from WRF have been coarse-grained to match the data resolution of the TRMM 3B42 gridded product.

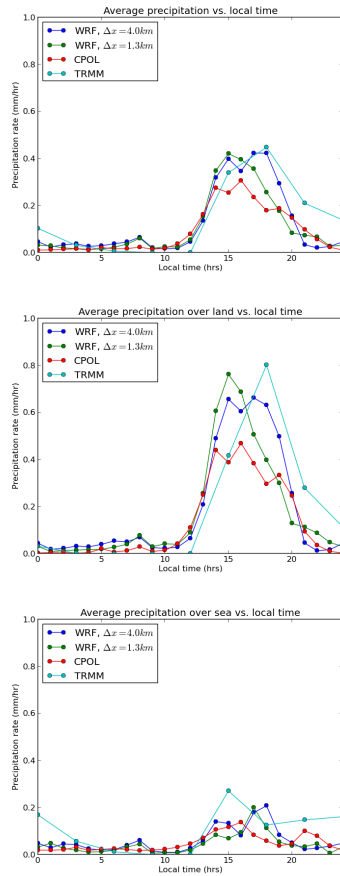


Figure 3. Comparison of simulated diurnal rainfall at 4 and 1.33 km resolutions with TRMM and radar-derived precipitation (CPOL) around Darwin, Australia, area-averaged over the entire horizontal coverage (top), over land (middle) and over sea points (bottom) within the radar domain, respectively. The mean diurnal cycle is composited using days 02–09 and 11–12 February.

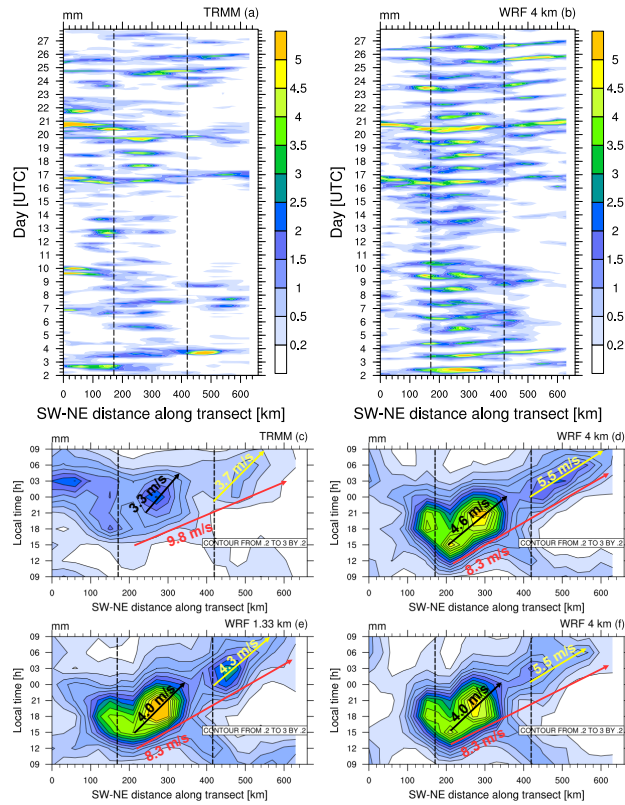


Figure 4. Time-distance plots of 3 hourly mean rainfall, averaged across the line sections in Fig. 1a, from (a) TRMM and (b) 4 km WRF for the period 02–28 February 2010. The mean diurnal cycle in local time, composited using 3 hourly data, is also shown for (c) TRMM, (d) 4 km (re-initialized runs), (e) 1.33 km and (f) 4 km two-week free-running WRF runs. Vertical dashed lines represent the positions of the averaged mountain peak (about 170 km) and northern coastline (about 420 km), respectively. Coloured lines show the estimated phase speeds for the peak rain signals over land (black), over water (yellow) and for the broader rain envelope (red).

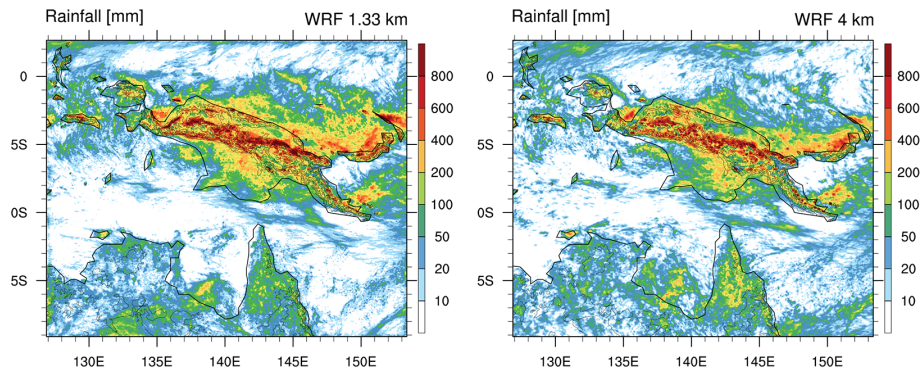


Figure 5. Two-week rainfall accumulations from the (a) 1.33 km and (b) 4 km free-running model simulations in domain 3 (d03) at their native grid resolutions.

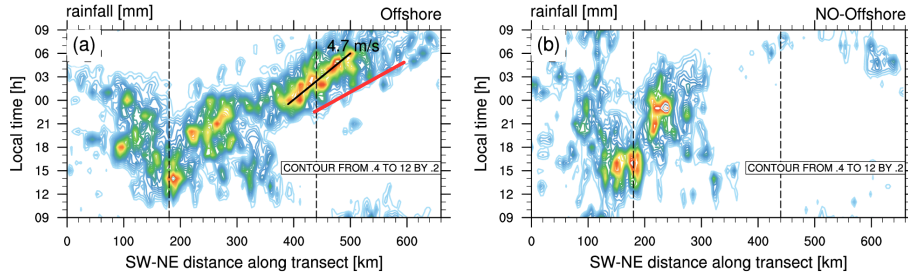


Figure 6. Composite diurnal cycle in local time (LT) in simulated (a) Offshore and (b) NO-Offshore days, as averaged across the line sections seen in Fig. 1a. The black line represents the estimated phase speed of the peak rain signal across the northern coast, while the red line denotes the estimated phase speed of the broader rain envelope ($\sim 8 \text{ m s}^{-1}$).

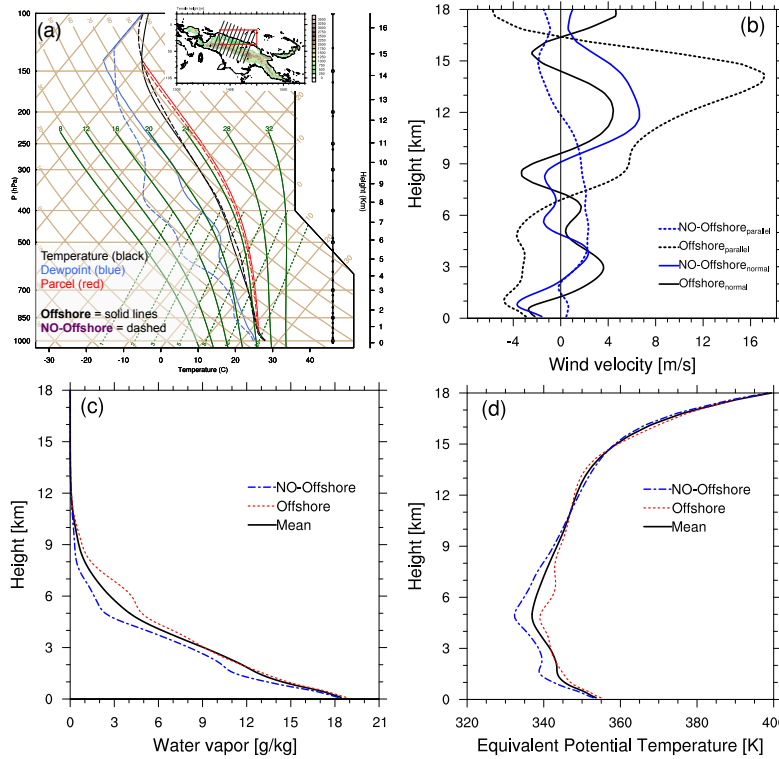


Figure 7. Mean profiles averaged within the region denoted by the red box in the inset. (a) Simulated temperature (black), dewpoint (blue) and parcel temperature (red) averaged for Offshore (solid) and NO-Offshore (dashed) days. (b) Vector wind in the direction normal (solid) and parallel (dashed) to the coast on Offshore (black) and NO-Offshore (blue) days. Positive values of normal velocity flow towards the north-northeast and parallel velocity flow towards the west-northwest. (c) Water vapour mixing ratio (g kg^{-1}) and (d) equivalent potential temperature (K) for Offshore and NO-Offshore days compared to the February mean.

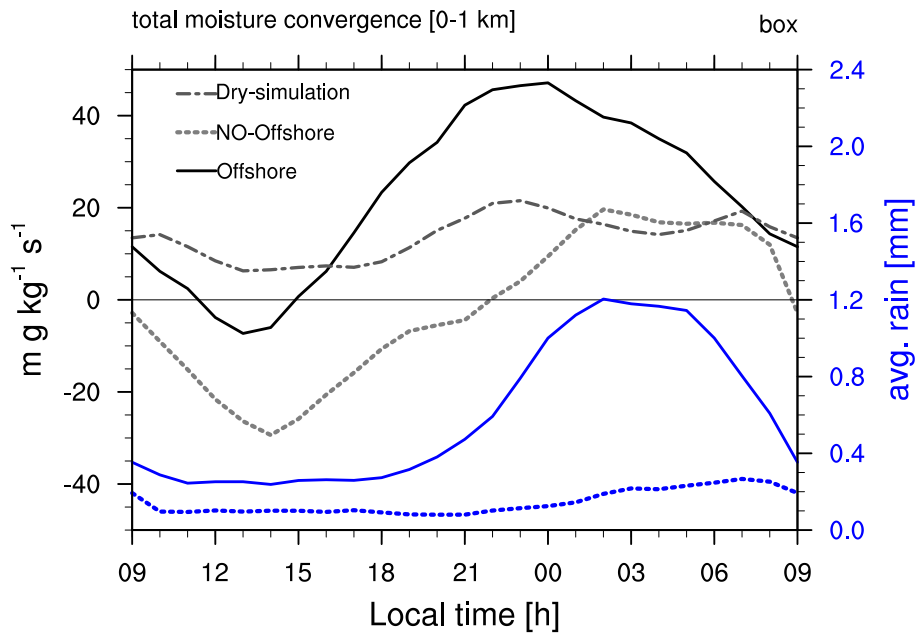


Figure 8. Total moisture convergence (VIMFC, $\text{m g kg}^{-1} \text{s}^{-1}$), vertically-integrated between surface and 1 km height (first 11 model levels), for the red box region shown in Fig. 7a (black lines). Area of the box is $290\,048 \text{ km}^2$ (88×206 grid points). The diurnal area-averaged rainfall for Offshore and NO-Offshore days are shown by the solid and dotted blue lines, respectively.

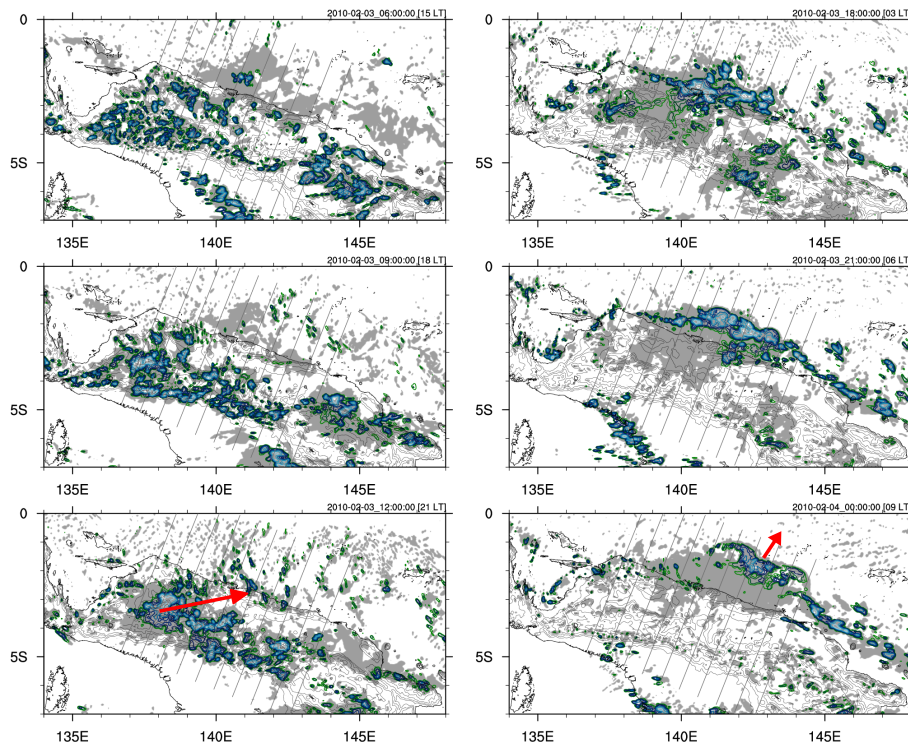


Figure 9. Multi-stage evolution of offshore squall-line propagation for a modelled storm on 03 February 2010, as shown by total column cloud (grey shade) and rainfall (green-blue contours) during the early evening (left panels) and early morning (right panels). The red arrows indicate the approximate direction of storm motion over land and water.

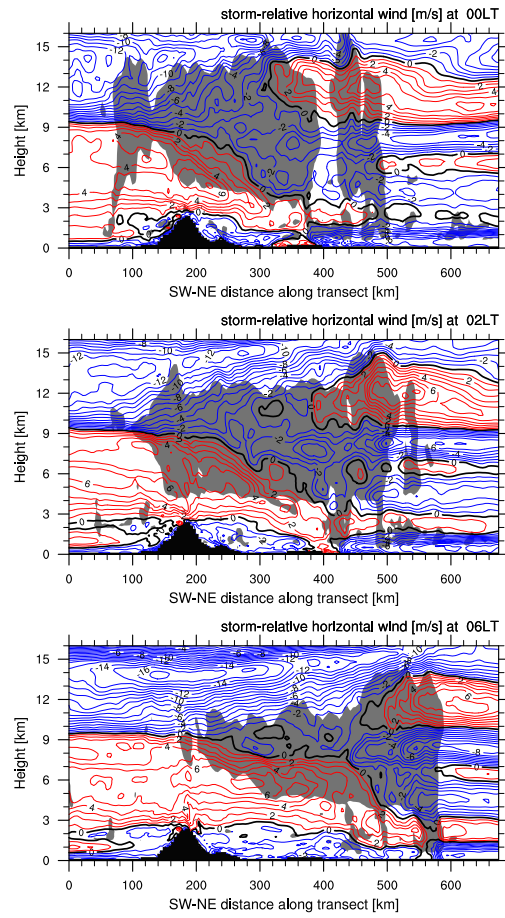


Figure 10. Mean system-relative horizontal wind along the section, as averaged across the transects seen in Fig. 1a at **(a)** 00:00 LT, **(b)** 02:00 LT and **(c)** 06:00 LT for a modelled system on 03 February 2010. Red is positive. Total cloud $\geq 0.05 \text{ g kg}^{-1}$ is shaded grey.

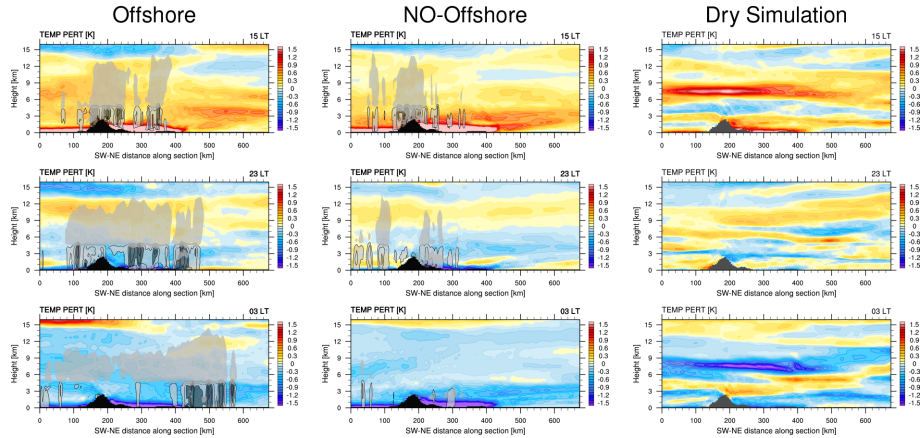


Figure 11. Temperature perturbations from daily mean (colours) for Offshore (left panels), NO-Offshore (middle panels) and Dry Simulation (right panels) at 15:00, 23:00 and 03:00 LT. Total condensate greater 0.05 g kg^{-1} is shaded grey, rain areas are contoured every 0.05 g kg^{-1} in black with regions greater than 0.15 g kg^{-1} shaded dark grey. The averaged terrain profile is shaded black.

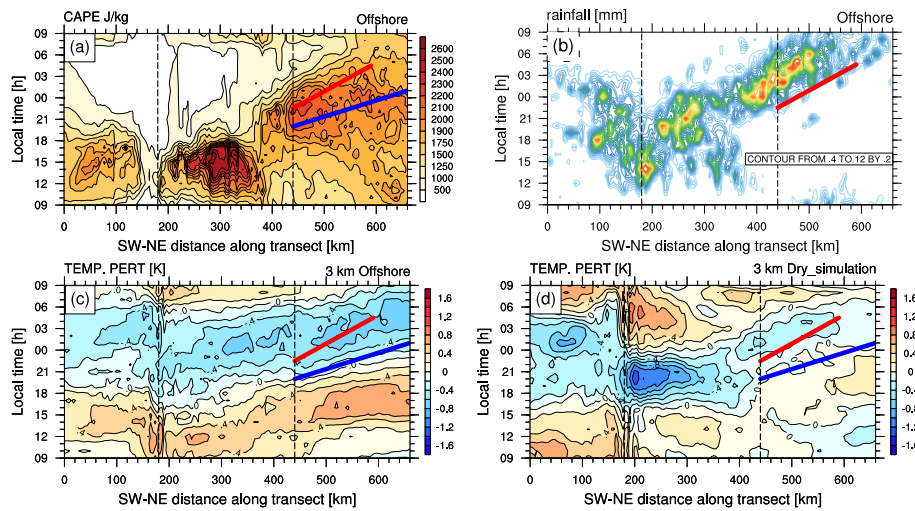


Figure 12. Mean diurnal cycles of (a) CAPE, (b) rainfall and (c) temperature perturbations from daily mean for Offshore days. (d) As in (c) but for the Dry simulation. Dashed vertical lines indicate the position of the ridge and northern coastline, respectively. The phase speed of the red line (denoting rainfall onset) is $\sim 8 \text{ m s}^{-1}$ while the phase speed of the blue line (denoting cooling onset) is $\sim 15 \text{ m s}^{-1}$.